

# A COMPARISON OF SIMPLE MASS ESTIMATORS FOR GALAXY CLUSTERS

TEREASA G. BRAINERD<sup>1</sup>, CANDACE OAXACA WRIGHT<sup>1</sup>,  
 DAVID M. GOLDBERG<sup>2</sup>, & JENS VERNER VILLUMSEN<sup>3</sup>

<sup>1</sup>) Boston University, Department of Astronomy, Boston, MA 02215

<sup>2</sup>) Princeton University, Department of Astrophysical Science, Princeton, NJ, 08544

<sup>3</sup>) Current postal address: 5151 Reed Road, Suite 224C, Columbus, OH 43220

*Accepted for publication in The Astrophysical Journal*

## ABSTRACT

High-resolution N-body simulations are used to investigate systematic trends in the mass profiles and total masses of clusters as derived from 3 simple estimators: (1) the weak gravitational lensing shear field under the assumption of an isothermal cluster potential, (2) the dynamical mass obtained from the measured velocity dispersion under the assumption of an isothermal cluster potential, and (3) the classical virial estimator. The clusters used for the analysis were obtained from simulations of a standard cold dark matter universe at  $z = 0.5$  and consist of order  $2 \times 10^5$  to  $3 \times 10^5$  particles of mass  $m_p \simeq 10^{10} M_\odot$ . The clusters are not smooth and spherically symmetric but, rather, the mass distribution is triaxial and significant substructure exists within the clusters. Not surprisingly, the level of agreement between the cluster mass profiles obtained from the various estimators and the actual mass profiles is found to be scale-dependent.

We define the total cluster mass to be the mass contained within a 3-dimensional radius  $r_{200}$  of the cluster centers, where  $r_{200}$  is the radius inside which the mean interior overdensity is equal to 200. Under this definition the classical virial estimator yields a good measurement of the total cluster mass, though it is systematically underestimated by  $\sim 10\%$ . This result suggests that, at least in the limit of ideal data, the virial estimator is quite robust to deviations from pure spherical symmetry and the presence of substructure within a cluster. The dynamical mass estimate based upon a measurement of the cluster velocity dispersion and an assumption of an isothermal potential yields a poor measurement of the total cluster mass, underestimating it by  $\sim 40\%$  for the case that  $\sigma_v$  is computed from an average over the entire cluster. The weak lensing estimate yields a very good measurement of the total cluster mass, provided the mean shear used to determine the equivalent cluster velocity dispersion is computed from an average of the lensing signal over the entire cluster (i.e. the mean shear is computed interior to a projected cluster radius of  $R_{200}$ ).

*Subject headings:* cosmology: theory — dark matter – gravitational lensing — large-scale structure of the Universe — galaxies: clusters: general — methods: numerical

## 1. INTRODUCTION

Rich clusters of galaxies constitute the largest gravitationally-bound objects in the universe and the history of their formation is a potentially powerful test of the viability of differing large-scale structure models. In particular, the time evolution of the cluster mass function is expected to be a good discriminator between low- and high-density universes, and, additionally, it provides a constraint on the degree of bias between the galaxy and mass distribution (e.g. Bahcall et al., 1997; Fan et al., 1997). Owing to the lack of complete, uniform, mass-selected catalogs of galaxy clusters out to large depths ( $z \sim 0.5$  to 1.0), the evolution of the cluster mass function is not constrained especially well at present. It is expected, however, that significant effort will soon be devoted to developing such catalogs, particularly using deep wide-field imaging of weak gravitational lensing of distant field galaxies by intervening clusters. The ability of these future catalogs to constrain models of structure formation rests heavily on the accuracy with which the cluster masses can be obtained and an understanding of any systematic biases present in the mass estimators themselves.

The virial mass estimator is the method which has the longest history of application to galaxy clusters and it yields consistent results for cluster mass to light ratios in the range of  $200h(M/L)_\odot$  to  $400h(M/L)_\odot$  (e.g. Zwicky 1933, 1937; Smith 1936; Schwarzschild 1954; Gott & Turner 1976; Gunn 1978; Ramella, Geller & Huchra 1989; David, Jones & Forman 1995; Bahcall, Lubin & Dorman 1995; Carlberg et al. 1996; Carlberg, Yee & Ellingson 1997). While there are legitimate concerns that large clusters are not fully virialized, Carlberg et al. (1997a) have presented spectroscopic evidence which strongly suggests that the clusters in the CNOC survey are in equilibrium and, therefore, that the masses obtained within the virial radius are reliable.

Nevertheless, because of its potential power to map the dark mass distribution within a cluster independent of the cluster's dynamical state, recently a great deal of effort has been devoted to measurements of the gravitational potentials of clusters via observations of weak lensing (e.g. Tyson, Wenk & Valdes 1990; Bonnet et al. 1994; Dahle, Maddox & Lilje 1994; Fahlman et al. 1994; Mellier et al. 1994; Smail et al. 1994, 1995, 1997; Tyson & Fischer 1995; Smail & Dickinson 1995; Kneib et al 1996; Seitz et al.

1996; Squires et al. 1996ab; Bower & Smail 1997; Fischer et al. 1997; Fischer & Tyson 1997; Luppino & Kaiser 1997). Relatively few clusters have been studied in detail, but a consistent picture of the dark mass distribution appears to be emerging from the weak lensing investigations. In particular, the center of mass corresponds well with the center of the optical light distribution and the smoothed light distribution traces the dark mass well. The lensing-derived mass to light ratios vary from cluster to cluster but bracket a broad range of  $200h(M/L)_{\odot}$  to  $800h(M/L)_{\odot}$ , with most of the clusters falling in the middle of the range.

The consistency of cluster masses obtained from independent methods such as lensing, virial analyses, or X-ray data (assuming pressure supported hydrostatic equilibrium) is very much in debate at this time. Cluster mass estimates obtained from observations of strong lensing can often exceed the X-ray mass by a factor of 2 to 3 (e.g. Miralda-Escudé & Babul 1995). This particular discrepancy is likely due to the failure of the assumption of hydrostatic equilibrium and Waxman & Miralda-Escudé (1995) have thus proposed the existence of multiphase cooling flows in the centers of rich clusters. Based on analyses of weak lensing over considerably larger cluster radii, however, some studies conclude that there is quite good agreement between the lensing and X-ray masses (e.g. Squires et al. 1996ab; Smail et al. 1997) while others claim a significant disagreement in which the lensing mass systematically exceeds the X-ray mass (e.g. Fischer et al. 1997; Fischer & Tyson 1997). Additionally, the weak lensing mass estimate is often found to exceed the mass obtained from the virial estimator by a factor of order 2 (e.g. Fahlman et al. 1994; Carlberg et al. 1994; Smail et al. 1997) but in some cases good agreement between these two independently derived masses is found (e.g. Fischer et al. 1997).

One of the troubles associated with a fair assessment of independent cluster mass estimates is that different techniques tend, out of necessity, to be applied at different cluster radii (i.e. it is not always possible to investigate the gravitational potential over the entire cluster via one particular estimator simply due to lack of data on appropriate scales). Systematic biases inherent in any given mass estimator may well be scale-dependent and amongst different estimators the form of the scale dependence is likely to vary. Therefore, a considerable effort will be required in order to reconcile all of the outstanding discrepancies amongst independent cluster mass estimates.

Few observational investigations have been able to place direct constraints on the radial mass profiles of clusters to date. Bonnet et al. (1994) detected a coherent weak lensing shear due to the cluster Cl0024+1654 out to a radius of  $r \sim 1.5h^{-1}$  Mpc and from their observations they showed that the underlying cluster mass profile was consistent both with an isothermal profile and a steeper de Vaucouleurs profile. Similarly, Fischer & Tyson (1997) found that the weak lensing shear field of RXJ 1347.5-1145 yielded a density profile that was consistent with isothermal. Tyson & Fisher (1995), however, found that the density profile implied by weak lensing observations of A1689 was steeper than isothermal on large scales ( $200h^{-1}\text{kpc} \lesssim r \lesssim 1h^{-1}\text{Mpc}$ ). Similarly, Squires et al. (1996b) found that the density profile of A2390 implied by the weak lensing shear field was consistent with isothermal on small scales ( $r \lesssim 250h^{-1}\text{kpc}$ ), but on larger scales

was better described by a profile steeper than isothermal. In contrast to the weak lensing results, however, Carlberg et al. (1997b) found that the velocity dispersion profiles of the CNOC clusters gave rise to a mean cluster mass profile that was fit very well by a Navarro, Frenk & White profile, i.e. shallower than isothermal at small radii and isothermal at large radii (e.g. Navarro, Frenk & White 1995, 1996, 1997).

In this investigation we use high-resolution N-body simulations of rich clusters to investigate systematic trends in both the total cluster masses and the radial mass profiles as derived from three simple estimators: (1) the weak lensing shear field under the assumption of an isothermal cluster potential, (2) the dynamical mass obtained from the measured velocity dispersion under the assumption of an isothermal cluster potential, and (3) the classical virial estimator. The simulated clusters are very massive and thus do not constitute an average, unbiased sample of objects. They do, however, correspond to the largest clusters likely to form in a standard CDM universe and are objects which would certainly be detectable as weak gravitational lenses. The N-body simulations of the clusters are discussed in §2 and the weak lensing and dynamical properties of the clusters are discussed in §3 together with the mass profiles obtained from the three estimators. A discussion of the results is presented in §4.

## 2. THE NUMERICAL CLUSTERS

The Hierarchical Particle-Mesh (HPM) N-body code written by J. V. Villumsen (Villumsen 1989) was used to simulate the formation of three rich clusters. The HPM code allows small-volume particle-mesh simulations to be nested self-consistently within large-volume particle-mesh simulations and by successively nesting many simulations within each other it is possible to obtain extremely high resolution in both mass and length within a small, localized region of a large computational volume (a “power zoom” effect). The code is, therefore, especially useful for the simulation of the formation of objects such as individual clusters. In particular, using the HPM code to simulate the formation of clusters obviates the need for computations which utilize “constrained initial conditions” and those which simulate at high resolution the evolution of density peaks that have been excised from the initial conditions of a large computational volume. While the largest-volume, lowest-resolution grid in an HPM simulation uses periodic boundary conditions, the smaller-volume, higher-resolution grids use isolated boundary conditions, allowing mass to flow in and out of the higher-resolution grids over the course of the simulation. Therefore, unlike constrained initial conditions or peak-excision simulations, clusters simulated with HPM are guaranteed to accrete all of the mass that they should accrete if one simply ran a single large-volume simulation at a level of resolution comparable to that of the highest-resolution HPM grid.

The HPM code uses a standard cloud-in-cell (CIC) interpolation scheme, which results in an approximately Gaussian smoothing of the power spectrum with a smoothing length of  $r_s = 0.8$  grid cell (see, e.g., §6.6 of Blandford et al. 1991). The gravitational force is, therefore, softer than Newtonian on small scales but becomes Newtonian for length scales greater than or of order 2 grid cells (Villumsen 1989). Due to the force softening we therefore

restrict our analyses to length scales greater than 2 grid cells.

The clusters used for the present analysis are discussed in detail in Brainerd, Goldberg & Villumsen (1998) and here we present only a summary of the simulations involved. A standard Cold Dark Matter model ( $\Omega_0 = 1$ ,  $\Lambda_0 = 0$ , and  $H_0 = 50$  km/s/Mpc) was adopted and the present epoch (i.e. redshift,  $z$ , of 0) was taken to correspond to  $\sigma_8 = 1$  where

$$\sigma_8 \equiv \left\langle \left[ \frac{\delta\rho}{\rho} (8h^{-1}\text{Mpc}) \right]^2 \right\rangle^{\frac{1}{2}}. \quad (1)$$

This is a model which is somewhat under-normalized compared to the COBE observations (e.g. Bunn & White 1997) and over-normalized compared to the abundance of rich clusters (e.g. Bahcall & Cen 1993; White, Efstathiou & Frenk 1993; Eke, Cole & Frenk 1996; Viana & Liddle 1996). The simulations began at  $\sigma_8 = 0.033$  (corresponding to a redshift of 29) and were evolved forward in time to  $\sigma_8 = 1.0$ .

The formation of the three most massive (i.e. “richest”) clusters contained within a single cubical volume of comoving side length  $L = 400$  Mpc was followed at high resolution. The large, primary computational volume common to all three clusters was a standard particle-mesh simulation consisting of  $256^3$  grid cells and  $128^3$  particles. Each cluster in turn was simulated at increased resolution by nesting two smaller, higher-resolution grids successively within the large, primary simulation volume. These two small, higher-resolution grids were centered on the center of mass of the particular cluster being simulated, used  $256^3$  grid cells each and had comoving side lengths of  $L = 66.6$  Mpc and  $L = 16.7$  Mpc, respectively. Since isolated boundary conditions are used in the small-volume simulations, the number of particles physically inside the small grids varied over the course of the simulations.

The particle mass in the large computational volume common to all three clusters was  $m_p = 2.1 \times 10^{12} M_\odot$ , while for the smaller grids unique to the individual clusters, the particle masses were  $m_p = 7.8 \times 10^{10} M_\odot$  and  $m_p = 9.8 \times 10^9 M_\odot$  in the grids with  $L = 66.6$  Mpc and  $L = 16.7$  Mpc, respectively. Dynamic ranges of  $\sim 4.5 \times 10^8$  in mass and  $\sim 6000$  in length were thus achieved by nesting the smaller simulations within the primary computational volume.

Throughout the present analysis we shall define the clusters to consist of all particles within a radius  $r_{200}$  of the centers of mass, where  $r_{200}$  is the radius inside which the mean interior mass overdensity is 200:

$$\frac{\delta\rho}{\rho}(r_{200}) = 200 \quad (2)$$

(see, e.g., Navarro, Frenk & White 1997, 1996, 1995). The cluster mass estimates were computed using only particles from the three highest-resolution grids (i.e. the grids with  $L = 16.7$  Mpc and  $m_p = 9.8 \times 10^9 M_\odot$ ) at an epoch corresponding to a redshift of 0.5 ( $\sigma_8 = 0.67$  for our normalization). All of the particles within  $r_{200}$  of the cluster centers were excised from the highest-resolution grid and were then used to compute the mass profiles. The total number of particles per cluster located within  $r_{200}$  at

$z = 0.5$  are: 192346 (“cluster 1”;  $r_{200} = 2.1$  Mpc, proper radius), 288641 (“cluster 2”;  $r_{200} = 2.4$  Mpc, proper radius), and 310310 (“cluster 3”;  $r_{200} = 2.5$  Mpc, proper radius). Within  $r_{200}$  the clusters contain a significant amount of substructure and have median projected ellipticities of 0.3. Cluster 1 is nearly prolate while clusters 2 and 3 are nearly oblate. Although the density profiles of the clusters are fit well by Navarro, Frenk, & White (1997, 1996, 1995) profiles, the values of the best-fit concentration parameters obtained for the clusters are a factor of order 2 lower than the values predicted by the Navarro, Frenk & White formalism for objects in the identical mass range. For a full discussion of the above cluster properties see Brainerd, Goldberg & Villumsen (1998).

### 3. RESULTS

Two-dimensional projections of the clusters are shown in the top panels of Figs. 1, 2, and 3. The color scale shows the logarithm of the surface mass density (in units of  $M_\odot/\text{kpc}^2$ ) and distances are given in proper coordinates for  $z = 0.5$ . The actual mass profiles of the clusters are shown in Fig. 4, where the top panel shows the mean 2-dimensional projected mass profile obtained from 10 random projections of each cluster and the bottom panel shows the 3-dimensional mass profile of each cluster. Throughout we shall adhere to notation in which  $R$  refers to a proper radius projected on the sky and  $r$  refers to a 3-dimensional proper radius. In this notation, then,  $M(R)$  is the projected mass interior to a radius  $R$  on the sky and  $M(r)$  is the mass interior to a sphere of radius  $r$ . As expected from the work by Navarro, Frenk & White (1997, 1996, 1995) on the relatively generic shapes of the density profiles of objects formed by dissipationless collapse, the mass profiles of the numerical clusters are not fit well by single power laws (see also Dubinski & Carlberg 1991, Cole & Lacey 1996, and Tormen, Bouchet & White 1997). Rather, a gently changing slope is observed, with the density profiles becoming roughly isothermal on large scales ( $\gtrsim 1$  Mpc in the case of our clusters).

Figs. 1, 2 & 3 are very large and have been omitted.

Fig. 1: Top panel: the logarithm of the surface mass density of cluster 1 as observed from a randomly-chosen line of sight. The units of the surface mass density are  $M_\odot/\text{kpc}^2$ . The cluster consists of all particles in the highest-resolution subgrid that are located within a radius  $r_{200}$  of the center of mass. Bottom panel: the gravitational lensing shear,  $\gamma$ , obtained for the projected mass density shown in the top panel. The cluster was placed at a redshift of 0.5 and the shear that would be in-

duced in a plane of sources at  $z = 1.0$  was computed by tracing a regular grid of  $4 \times 10^6$  light rays through the cluster. The color scale indicates the local value of  $\log_{10} \gamma$  while the orientation of the sticks indicates the orientation of the shear,  $\varphi$ . For clarity, the mean orientation of the local shear is shown on a coarse  $10 \times 10$  grid. The angular scale of the figure is of order  $11' \times 11'$ . Figs. 2 and 3 are the same as Fig. 1, but for clusters 2 and 3, respectively.

In the following subsections we will compare the true mass profiles of the clusters to the mass profiles obtained from the three estimators. All of the mass estimators assume the clusters to be spherically symmetric and, additionally, both the weak lensing and “isothermal” dynamical mass estimates assume that the cluster potential is approximately isothermal.

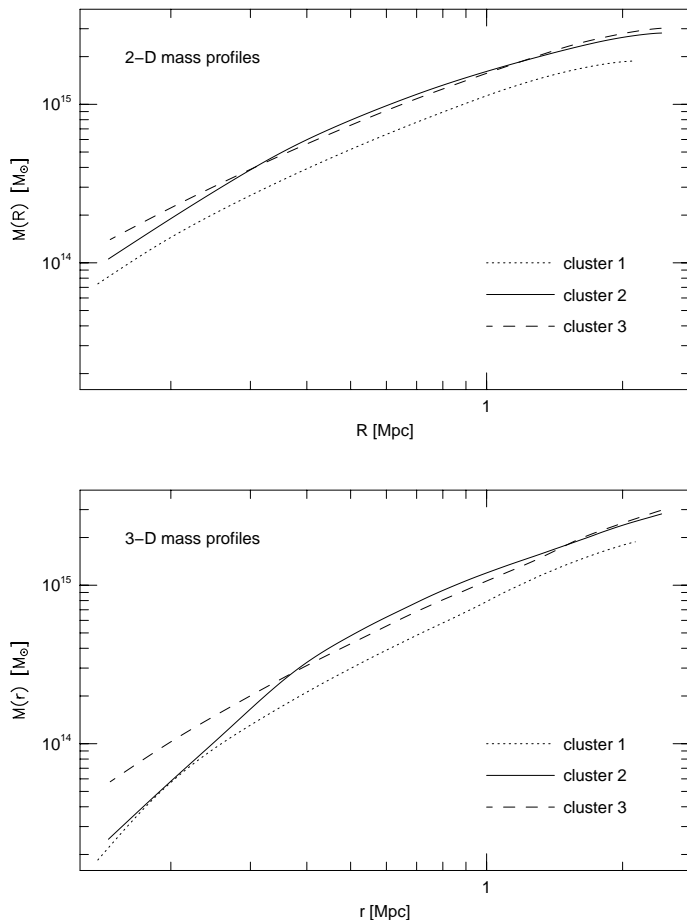


Fig. 4: The mass profiles of the clusters as computed directly from the distribution of particles in the highest-resolution grids. Top panel: the mean projected mass profile, computed from 10 random projections of each cluster. Bottom panel: the full 3-dimensional mass profile. The clusters are roughly isothermal on scales  $\gtrsim 1$  Mpc.

### 3.1. Weak Lensing Shear

Observations of gravitational lensing provide potentially powerful constraints on both the total mass and the mass distribution within clusters of galaxies. The gravitational potential of the cluster systematically deforms the shapes of distant source galaxies that are seen through the lensing cluster. The result is a net ellipticity induced in the images of lensed galaxies and a net tangential alignment of the lensed images relative to the center of the cluster

potential.

Provided the distance traveled by the light ray is very much greater than the scale size of the lens itself, it is valid to adopt the “thin lens approximation” in order to describe a gravitational lens. Consider a lens with an arbitrary 3-dimensional potential,  $\Phi$ . In the thin lens approximation a conveniently scaled 2-dimensional potential,  $\psi$ , is adopted for the lens (i.e.  $\psi$  is a scaled representation of the 3-dimensional potential of the lens integrated along the optic axis):

$$\psi(\vec{\theta}) = \frac{D_{ds}}{D_d D_s} \frac{2}{c^2} \int \Phi(D_d \vec{\theta}, z) dz. \quad (3)$$

Here  $\vec{\theta}$  is the location of the lensed image on the sky relative to the optic axis,  $D_{ds}$  is the angular diameter distance between the lens (the “deflector”) and the source,  $D_d$  is the angular diameter distance between the observer and the lens, and  $D_s$  is the angular diameter distance between the observer and the source.

Having adopted this 2-dimensional lens potential, then, it is straightforward to relate the potential of the lens (through second derivatives of  $\psi$ ) directly to the two fundamental quantities which characterize the lens: the convergence ( $\kappa$ ) and the shear ( $\vec{\gamma}$ ). The convergence, which describes the isotropic focusing of light rays, is given by:

$$\kappa(\vec{\theta}) = \frac{1}{2} \left( \frac{\partial^2 \psi}{\partial \theta_1^2} + \frac{\partial^2 \psi}{\partial \theta_2^2} \right). \quad (4)$$

The shear describes the tidal gravitational forces acting across a bundle of light rays and, therefore, the shear has both a magnitude,  $\gamma = \sqrt{\gamma_1^2 + \gamma_2^2}$ , and an orientation,  $\varphi$ . In terms of  $\psi$ , the components of the shear are given by:

$$\gamma_1(\vec{\theta}) = \frac{1}{2} \left( \frac{\partial^2 \psi}{\partial \theta_1^2} - \frac{\partial^2 \psi}{\partial \theta_2^2} \right) \equiv \gamma(\vec{\theta}) \cos [2\varphi(\vec{\theta})] \quad (5)$$

$$\gamma_2(\vec{\theta}) = \frac{\partial^2 \psi}{\partial \theta_1 \partial \theta_2} = \frac{\partial^2 \psi}{\partial \theta_2 \partial \theta_1} \equiv \gamma(\vec{\theta}) \sin [2\varphi(\vec{\theta})] \quad (6)$$

(e.g. Schneider, Ehlers & Falco 1992).

A great deal of work has been done in recent years to develop methods by which a map of the surface mass density of a cluster can be reconstructed from observations of the distortions induced in the images of background galaxies in the limit of weak gravitational lensing, for which  $\kappa \ll 1$  and  $|\gamma| \ll 1$  (e.g. Kaiser & Squires 1993; Bartelmann 1995; Kaiser 1995; Kaiser et al. 1995; Schneider 1995; Schneider & Seitz 1995; Seitz & Schneider 1995; Bartelmann et al. 1996; Seitz & Schneider 1996; Squires & Kaiser 1996; Seitz et al. 1998). It is not the intent of this paper to explore these detailed methods of cluster mass reconstruction. Rather, we will focus on a very simple weak lensing analysis technique that is sometimes used to gauge the total mass of a cluster contained within a given radius without fully reconstructing the underlying density profile.

The method invokes an assumption that the cluster potential may be represented adequately by an isothermal sphere. The actual density potentials of the numerical clusters are better represented by Navarro, Frenk & White profiles (see Brainerd, Goldberg & Villumsen 1998) than by singular isothermal spheres and, given the apparent

generality of the NFW profile, it is more likely that an NFW profile will better represent an actual galaxy cluster than will an isothermal sphere. Here we choose to adopt the isothermal sphere approximation for the analysis because this is the simplifying assumption that is most commonly invoked in the literature when cluster masses are estimated from observations of weak lensing without a full reconstruction of the density profile (see the references listed below). Here our goal is simply to quantify systematic effects due to the assumption of an underlying isothermal potential when the true potential is better approximated by that of an NFW-type object.

An isothermal sphere is uniquely specified by a single quantity, the velocity dispersion ( $\sigma_v$ ), and the mass of an isothermal sphere contained within a 3-dimensional radius  $r$  is given by

$$M(r) = \frac{2\sigma_v^2 r}{G} \quad (7)$$

where  $G$  is Newton's constant. The total mass of an isothermal sphere within a radius  $R$  projected on the sky is given by

$$M(R) = \frac{\pi\sigma_v^2 R}{G} \quad (8)$$

(e.g. Binney & Tremaine 1987).

Since it is spherically symmetric, the isothermal sphere gives rise to a gravitational lensing shear field which is necessarily circularly symmetric and, in particular, the shear as a function of angular radius,  $\theta$ , is given by

$$\gamma(\theta) = \frac{2\pi}{\theta} \left( \frac{\sigma_v}{c} \right)^2 \left[ \frac{D_{ds}}{D_s} \right], \quad (9)$$

where  $c$  is the velocity of light and  $\sigma_v$  is the velocity dispersion of the lens (e.g. Schneider, Ehlers & Falco 1992). If we consider an annulus of inner radius  $\theta_{\min}$  and outer radius  $\theta_{\max}$  centered on the center of mass of the isothermal sphere, the mean shear inside the annulus is given by

$$\bar{\gamma} = 4\pi \left( \frac{\sigma_v}{c} \right)^2 \left[ \frac{D_{ds}}{D_s} \right] (\theta_{\max} + \theta_{\min})^{-1}. \quad (10)$$

That is, provided the cluster potential is sufficiently well-represented by an isothermal sphere it is possible to deduce its characteristic velocity dispersion directly from either a measurement of the shear at a given radius,  $\gamma(\theta)$ , or the mean value of the shear,  $\bar{\gamma}$ , computed within some large annulus. A measurement of  $\sigma_v$  by such a technique then leads to an estimate of the mass of the cluster within a given radius (e.g. Tyson, Wenk & Valdes 1990; Bonnet et al. 1994; Smail et al. 1994, 1997; Smail & Dickinson 1995; Bower & Smail 1997; Fischer & Tyson 1997).

In practice, an observed weak lensing shear only places a limit on the mass of cluster to within an additive constant (the so-called uniform density mass sheet degeneracy). The simple singular isothermal sphere mass estimator that we use here formally assumes that there is no such mass sheet present and that the observed weak lensing shear can be directly translated into a mass measurement via equations (7), (8), (9), and (10). Below we will, therefore, interpret the cluster shear fields in a manner consistent with the simple form of the mass estimator and we will not explicitly address the mass sheet degeneracy

problem or its implications for an observed weak lensing shear.

In this section we compute the shear fields of the numerical clusters and in §3.3 we will use these shear fields to investigate the systematic effects that the above weak lensing mass estimate has on the masses inferred for the numerical clusters. The shear fields of the clusters are determined directly by tracing regular Cartesian grids of  $2001 \times 2001$  light rays through the clusters. In the analysis below we adopt the thin lens approximation and for a particular plane projection of a cluster we simply calculate the net deflection of each light ray due to all of the point masses contained within  $r_{200}$  of the cluster center of mass. Note, however, that we ran a few test cases in which all particles inside a radius of 4 Mpc of the cluster centers were included in the ray trace analysis. The inclusion of the mass exterior to a radius of  $r_{200}$  gave rise to a shear field interior to  $r_{200}$  that was indistinguishable from the shear field obtained using only the particles interior to  $r_{200}$ . That is, owing to the fact that the clusters are roughly axisymmetric and no large mass concentrations exist just outside the clusters, the shear interior to a projected radius  $R$  is determined by the surface mass density interior to  $R$ .

The clusters are located at a redshift of  $z = 0.5$  and we consider a plane of sources at  $z = 1.0$ . (Although the redshift of the sources will affect the magnitude of the shear, it will not affect the velocity dispersion inferred in the isothermal sphere approximation and, therefore, the choice of source plane is essentially arbitrary for our analysis.) The side lengths of the grids of light rays were taken to be  $L = 2r_{200}$  so that throughout we compute only the shear interior to the virial radii of the clusters. At the redshift of the clusters, then, the side lengths of the grids correspond to an angular scale of order  $11' \times 11'$ .

If we let the location of a light ray on the grid be given by  $\vec{\beta}$  prior to lensing (i.e.  $\vec{\beta}$  is the location of the light ray in the source plane) and we let  $\vec{\theta}$  be the location of the light ray after having been lensed by all of the point masses (i.e.  $\vec{\theta}$  is the location of the light ray in the image plane), the components of the shear are then given by:

$$\gamma_1(\vec{\theta}) = -\frac{1}{2} \left( \frac{\partial \beta_x}{\partial \theta_x} - \frac{\partial \beta_y}{\partial \theta_y} \right) \quad (11)$$

$$\gamma_2(\vec{\theta}) = -\frac{1}{2} \left( \frac{\partial \beta_x}{\partial \theta_y} + \frac{\partial \beta_y}{\partial \theta_x} \right) \quad (12)$$

The  $2001 \times 2001$  light rays define a grid of  $2000 \times 2000$  cells and the shear at the centers of each of these cells can be determined from equations (11) and (12) above by finite differencing of the deflections of the four light rays which define the corners of the cell.

The code used to compute the net deflections of the grid of light rays was tested by tracing the light rays through a number of singular isothermal spheres that were approximated by a set 250,000 point masses. The point masses were constrained to lie within a maximum projected radius of  $R = 2.7$  Mpc and their masses were scaled appropriately so as to reproduce the correct values of  $M(R = 2.7 \text{ Mpc})$  for a set of isothermal spheres with values of  $\sigma_v$  in the range of 500 km/s to 1500 km/s. As with the simulated clusters, the isothermal sphere lenses were placed at

$z = 0.5$  and the source light rays emanated from  $z = 1.0$ . The net deflections of the light rays were evaluated and the radial dependence of the convergence,  $\kappa(R)$ , and shear,  $\gamma(R)$ , was computed and compared to the analytic expectations for infinite singular isothermal spheres having values of  $\sigma_v$  identical to the isothermal spheres that were approximated by the point masses. For the isothermal sphere we know  $\kappa(R) = \gamma(R)$ , and in all cases good agreement was found between both  $\kappa(R)$  and  $\gamma(R)$  as computed individually from the ray tracing and between the ray tracing results and the analytic expectations (deviations  $\lesssim 1\%$  of the analytic values).

Shown in the bottom panels of Figs. 1, 2, and 3 are the shear fields corresponding to the 2-dimensional projections of the clusters shown in the top panels of these figures. The color scale shows the logarithm of the magnitude of the shear and the small sticks indicate its orientation. For clarity of the figure, we plot the mean orientation of the shear on a coarse  $10 \times 10$  grid that was computed from an unweighted average of the local shear vectors obtained from the differencing of the displacements of the light rays (i.e. the sticks show a rebinning of the original  $2000 \times 2000$  grid of shear vectors onto a  $10 \times 10$  grid). The visual agreement of the magnitude and orientation of the shear with the actual surface mass density of the clusters is as expected; the shear is greatest in the densest regions of the clusters and is oriented roughly tangentially with respect to the cluster centers. The shear fields are not, however, circularly symmetric and reflect both the overall ellipticity of the clusters and the substructure within them.

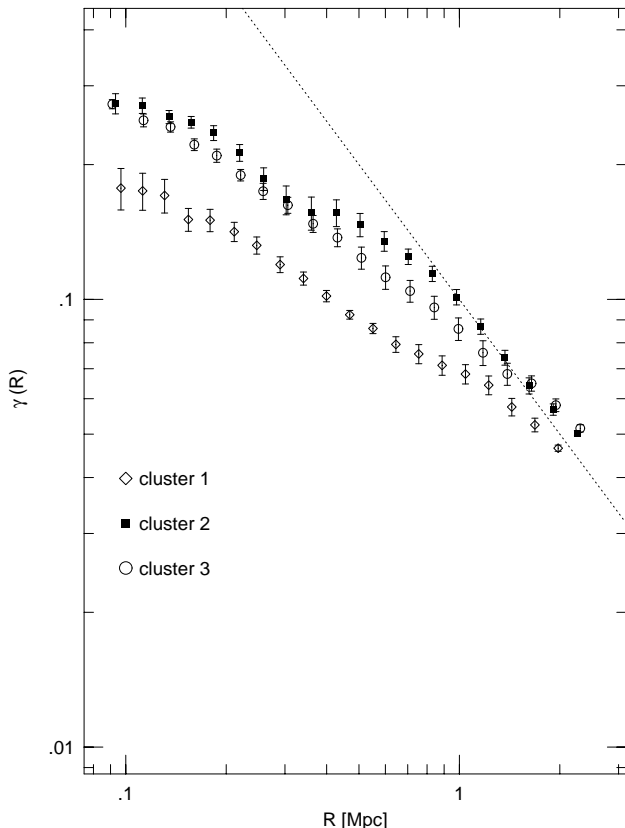


Fig. 5: The mean gravitational lensing shear for the clusters as a function of projected radius. Two-dimensional shear fields were determined for 10 random projections of each cluster, from which the average radial value of the shear was computed in independent bins of radius  $R$

centered on the cluster center of mass. The error bars show the formal standard deviation in the mean between the 10 projections. For comparison the dotted line indicates the shape of the shear profile expected for an isothermal sphere lens,  $\gamma(R) \propto R^{-1}$ .

Each cluster was viewed at 10 random orientations and a mean radial shear profile was computed from the full  $2000 \times 2000$  grid of shear vectors. The results are shown in Fig. 5, where the error bars indicate the formal standard deviation in the mean between the 10 random projections. Also shown for comparison is the radial shear profile expected for an isothermal sphere (i.e.  $\gamma(R) \propto R^{-1}$ , cf. equation 9 above). Below a scale of  $\sim 1$  Mpc the radial shear profiles of the clusters behave as  $\gamma(R) \propto R^{-0.5}$ , while on larger scales the variation of  $\gamma$  with  $R$  is roughly isothermal,  $\gamma(R) \propto R^{-1}$ . Given the mass profiles shown in Fig. 4, this is precisely the behavior we would anticipate for the shear profiles. This behavior will, however, cause systematic errors in the cluster masses inferred from the shear fields under the assumption of isothermal cluster potentials.

### 3.2. Velocity Dispersions

Under the assumption of an isothermal cluster potential, the masses of the clusters can be determined from measurements of their velocity dispersions alone (e.g. equations 7 and 8 above). The isothermal sphere is characterized by a single, constant value for the velocity dispersion and in this section we investigate the degree to which the measured cluster velocity dispersions vary with distance from the cluster centers of mass. The force resolution of the simulations is too poor to resolve convincingly the dark matter halos that would be associated with individual galaxies within the cluster (one grid cell in the particle-mesh calculation is of order 45 kpc in length) and, so, it is not possible to calculate the line of sight velocity dispersion of member galaxies directly. However, in the absence of significant velocity bias in both observed and high-resolution numerical clusters (e.g. Lubin & Bahcall 1993; Bromley et al. 1995; Ghigna et al. 1998), a random subset of the particles can be drawn from each cluster to estimate the velocity dispersion that would be expected for the member galaxies.

Each cluster was viewed from 1000 random orientations and the line of sight velocity dispersion,  $\sigma_v$ , was computed as a function of projected radius relative to the cluster center of mass. Two types of annuli were used for the computation: independent annuli (i.e.  $\sigma_v$  was computed in thin annuli with differential radius,  $R$ ) and cumulative annuli (i.e.  $\sigma_v$  was computed in wide annuli which shared a fixed inner radius,  $R_{\min}$ , and differed only by the maximum radius of the annuli,  $R_{\max}$ ). That is, the use of the independent annuli yields a measurement of  $\sigma_v$  at a particular projected distance from the cluster center while the use of the cumulative annuli yields a measurement of  $\sigma_v$  averaged over the entire cluster (out to some maximum radius). Throughout, the minimum radius from the cluster centers of mass,  $R_{\min}$ , was taken to be a distance equal to the length of two grid cells in the particle-mesh simulation since below that scale the gravitational force is softened by the N-body computational technique.

Shown in Figs. 6 and 7 (crosses) are the mean values of  $\sigma_v$  that were calculated directly from the line of sight velocities of particles within the clusters. Independent annuli

were used in Fig. 6 and cumulative annuli were used in Fig. 7. The error bars in the figure show the formal  $1\text{-}\sigma$  dispersion amongst the different projections of the clusters. The velocity dispersion computed using independent annuli decreases monotonically with radius in all three clusters but the decrease is slow enough such that averaged over large scales within the clusters (i.e.  $\sigma_v$  computed in the cumulative annuli) the velocity dispersion is roughly constant.

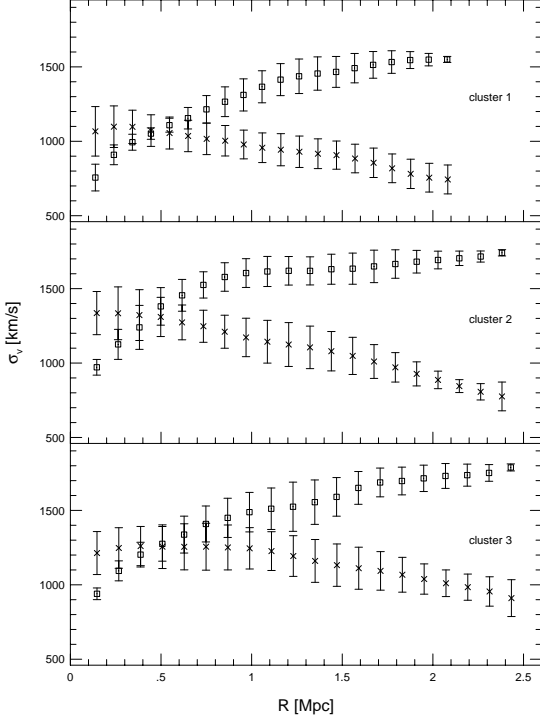


Fig. 6: Line of sight cluster velocity dispersions,  $\sigma_v$ , as function of projected radius. Crosses show the mean value of  $\sigma_v$  computed directly from the velocities of random subsets of the constituent particles and the error bars show the formal  $1\text{-}\sigma$  deviation amongst 1000 random lines of sight. Squares show the value of  $\sigma_v$  inferred for the clusters on the basis of the mean weak lensing shear, under the assumption that the cluster potential is well-represented by an isothermal sphere; error bars show the formal  $1\text{-}\sigma$  deviation amongst the 10 random lines of sight for which direct ray tracing was performed. In this figure  $\sigma_v$  has been computed using independent annuli with proper radius  $R$ .

Also shown in Figs. 6 and 7 (squares) are the mean values of  $\sigma_v$  that are *inferred* for the clusters on the basis of the weak lensing shear field, assuming that the cluster potentials can be well-represented by isothermal spheres (e.g. Fig. 5). From the 10 different projections for which direct ray tracing was performed, the mean shear was computed using both independent and cumulative annuli identical to the annuli used to compute the velocity dispersions of the particles themselves. The values of  $\gamma(R)$  and  $\bar{\gamma}(R_{\max})$  obtained from the ray trace analysis were then used in conjunction with equations (9) and (10) to infer the variation of the cluster velocity dispersion with radius. Error bars in Figs. 6 and 7 show the formal  $1\text{-}\sigma$  dispersion amongst the different cluster projections. In contrast to the velocity dispersion measured directly for the particles, the velocity dispersion inferred from the weak lensing analysis increases with radius monotonically.

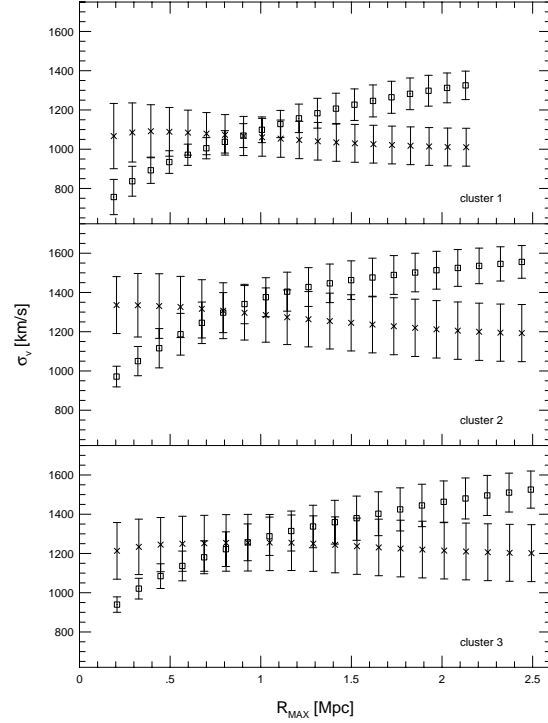


Fig. 7: Same as Fig. 6 except that in this figure  $\sigma_v$  has been computed using large cumulative radii of outer radius  $R_{\max}$  (see text).

### 3.3. Cluster Mass Estimates

Here we compute mass profiles for the clusters using the following simple estimators: (1) the mean value of the weak lensing shear under the assumption of an isothermal cluster potential, (2) the dynamical mass obtained from the line of sight velocity dispersion of the particles under the assumption of an isothermal cluster potential, and (3) the classical virial estimator. The cluster mass profiles obtained using the estimators are compared directly to the true mass profiles (e.g. Fig. 4) and throughout we will plot ratios of the estimated and true cluster mass profiles as a function of radius.

Shown in Figs. 8 and 9 are the mass profiles obtained from the mean weak lensing shear under the assumption of an isothermal cluster potential. Results for the 2-dimensional projected mass profiles are shown in Fig. 8 and the 3-dimensional mass profiles are shown in Fig. 9. The velocity dispersion,  $\sigma_v(R)$ , inferred from the circularly-averaged weak lensing signal (e.g. the squares in Fig. 6 and 7) was used in equations (7) and (8) above to compute  $M(r)_{\text{lens}}$  and  $M(R)_{\text{lens}}$ . In both Figs. 8 and 9 the circles indicate that the value of  $\sigma_v(R)$  was determined using the large, cumulative annuli (i.e. an average velocity dispersion over the cluster out to a maximum radius of  $R$ ). The solid squares in these figures indicate that the value of  $\sigma_v(R)$  was determined using thin, independent annuli (i.e. a value of the velocity dispersion computed at a particular distance,  $R$ , from the cluster center of mass). From the weak lensing analysis it is not possible to measure the direct dependence of  $\sigma_v$  on the 3-dimensional radius,  $r$ , and, so, to compute the 3-dimensional mass profile we have taken the velocity dispersion to be  $\sigma_v(r) \equiv \sigma_v(R = r)$ .

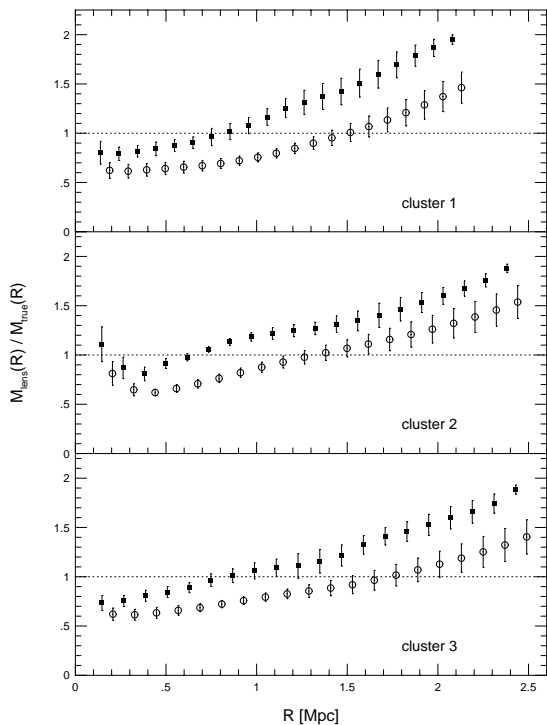


Fig. 8: The 2-dimensional, projected cluster mass profile obtained from the weak lensing analysis compared to the true cluster mass profile. Solid squares indicate that the value of  $\sigma_v$  used in equation (8) was determined from independent annuli of differential radius  $R$ ; open circles indicate that the value of  $\sigma_v$  was determined from large, cumulative annuli with outer radii of  $R_{\max} = R$ . The data points shown by the squares have been plotted such that  $R$  is the value of the projected radius at the mid-points of the independent radial bins and the data points shown by the circles are plotted such that  $R$  is the value of  $R_{\max}$  (i.e. for the circles  $R$  corresponds to the outermost radius of the annulus used in the calculation). Error bars show the  $1\text{-}\sigma$  dispersion in  $M(R)$  amongst the 10 different projections for which ray tracing was performed.

Fig. 8 shows that there is clearly a scale-dependent systematic deviation of the 2-dimensional projected cluster mass profile determined from the simple weak lensing analysis adopted here. Overall the trend is for  $M(R)_{\text{lens}}$  to increase monotonically with radius, underestimating the true projected mass at small radii and overestimating the true projected mass at large radii. The overestimate of the projected mass at large radii is simply a reflection of the fact that the isothermal sphere is, by definition, infinite in extent while the actual clusters are confined to a finite radius of  $r_{200}$ . (Note, however, that we performed a few test cases in which the proper radius of the numerical clusters was increased to a value of  $r = 4$  Mpc and this had a negligible effect upon the measured shear and, hence, the inferred projected mass.)

In contrast to the results for  $M(R)_{\text{lens}}$ , there is only a weak scale dependence in the deviation of  $M(r)_{\text{lens}}$  from the true 3-dimensional mass. Over most scales there is quite good agreement between the true cluster mass profiles and  $M(r)_{\text{lens}}$  as determined from values of  $\sigma_v$  that were computed using independent annuli. When values of  $\sigma_v$  determined from the large cumulative annuli are used,  $M(r)_{\text{lens}}$  systematically underestimates the true cluster

mass on scales significantly less than  $r_{200}$ . At large radii, however,  $M(r)_{\text{lens}}$  is in very good agreement with the true mass of the cluster for the case in which  $\sigma_v$  was determined from the large, cumulative annuli (i.e.  $\sigma_v$  is determined from the mean shear over the entire cluster). This result may seem a bit surprising given the fact that the clusters are better represented by NFW density profiles than they are by isothermal spheres. However, for NFW-type objects with masses comparable to those of our numerical clusters, the mean shear interior to  $R_{200}$  differs relatively little ( $\lesssim 10\%$ ) from that of an isothermal sphere that has an identical mass contained within  $r_{200}$  (Oaxaca Wright & Brainerd 1999). Hence, the isothermal sphere approximation should yield a reasonable estimate of the cluster mass contained within  $r_{200}$ , provided the mean shear is computed interior to a projected radius of  $R_{200}$ .

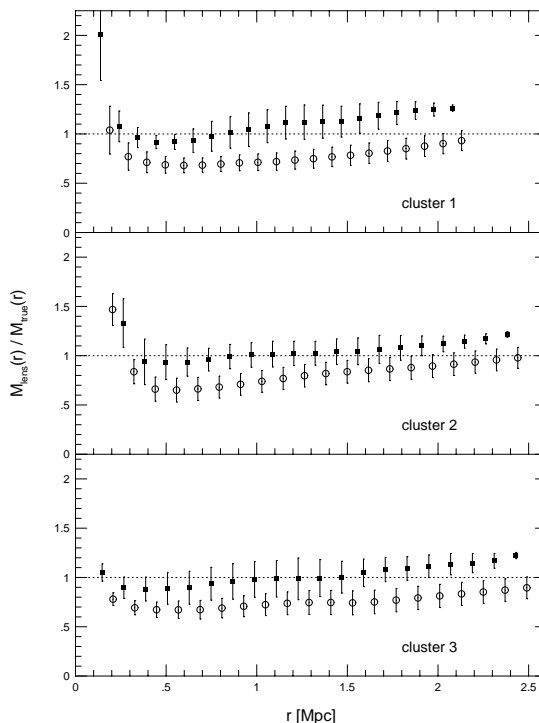


Fig. 9: The 3-dimensional cluster mass profile obtained from the weak lensing analysis compared to the true cluster mass profile. Solid squares indicate that the value of  $\sigma_v$  used in equation (7) was determined from independent annuli of differential radius  $R$ ; open circles indicate that the value of  $\sigma_v$  was determined from large, cumulative annuli with  $R_{\max} = r$ . The data points shown by the squares have been plotted such that  $r$  is the value of the 3-dimensional radius at the midpoints of the independent radial bins and the data points shown by the circles are plotted such that  $r$  is the value of  $r = R_{\max}$ . Error bars show the  $1\text{-}\sigma$  dispersion in  $M(r)$  amongst the 10 different projections for which ray tracing was performed.

Shown in Figs. 10 and 11 are the cluster mass profiles obtained from equations (7) and (8) in which  $\sigma_v$  is taken to be the mean particle velocity dispersion measured directly from random subsets of particles. The 2-dimensional projected mass profile,  $M_{\sigma_v}(R)$ , is shown in Fig. 10 and the 3-dimensional mass profile,  $M_{\sigma_v}(r)$ , is shown in Fig. 11. As in Figs. 8 and 9, circles refer to values of  $\sigma_v$  computed using the large cumulative annuli and squares refer to values of  $\sigma_v$  computed using the thin, independent annuli. Both the projected mass profiles and the 3-dimensional



mass profiles estimated directly from the particle velocity dispersions show scale-dependent deviations from the true mass profile. In this case the cluster mass is overestimated at very small radii and underestimated over most of the cluster.

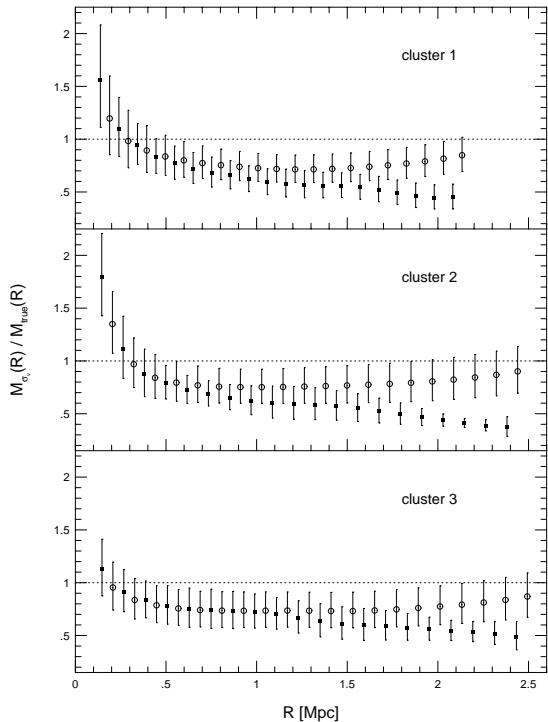


Fig. 10: The 2-dimensional, projected cluster mass profile obtained directly from the measured particle velocity dispersion (assuming the clusters to be isothermal spheres) compared to the true cluster mass profile. Solid squares indicate that the value of  $\sigma_v$  used in equation (8) was determined from independent annuli of differential radius  $R$ ; open circles indicate that the value of  $\sigma_v$  was determined from large, cumulative annuli with outer radii of  $R_{\text{max}} = R$ . Error bars show the  $1\text{-}\sigma$  dispersion in  $M(R)$  amongst the 1000 projections from which the mean line-of-sight velocity dispersion was computed.

Lastly, shown in Fig. 12 is a 3-dimensional mass profile computed for the clusters using a virial mass estimator. The classical cluster virial mass estimator is:

$$M = \frac{3\pi\sigma_v^2 R_e}{2G} \quad (13)$$

where  $R_e$  is the mean effective radius as projected on the sky:

$$R_e^{-1} \equiv \frac{1}{N^2} \sum_{i < j}^N \frac{1}{|\vec{R}_i - \vec{R}_j|} \quad (14)$$

and  $N$  is the number of galaxies in the cluster. Again, we cannot resolve the individual dark matter halos of member galaxies and, so, the virial analysis was performed on the clusters using random subsets of the particles. Particles contained within concentric spheres of radius  $r$  centered on the cluster centers of mass were viewed from 1000 random orientations and  $\sigma_v$  and  $R_e^{-1}$  were computed for each orientation. Values of  $r$  were increased incrementally to  $r_{\text{max}} = r_{200}$ , and  $M(r)$ , the mass contained within the concentric spheres, was computed using equation (13)

above. From Fig. 12, the virial mass estimator leads to a scale-dependent deviation from the true 3-dimensional mass profile in the sense that the cluster mass is overestimated on small scales. On large scales (and, in particular, near the “edges” of the clusters), however, the virial mass estimator reproduces the true cluster mass quite well.

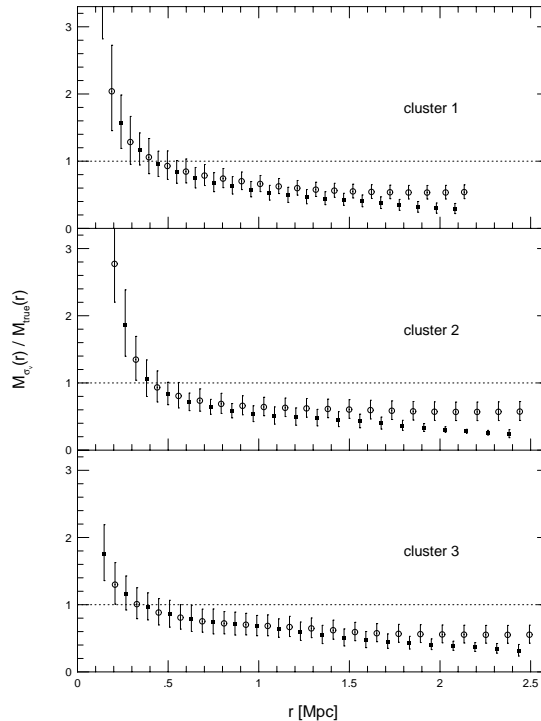


Fig. 11: The 3-dimensional cluster mass profile obtained directly from the measured particle velocity dispersion (assuming the clusters to be isothermal spheres) compared to the true cluster mass profile. Solid squares indicate that the value of  $\sigma_v$  used in equation (7) was determined from independent annuli of differential radius  $R$ ; open circles indicate that the value of  $\sigma_v$  was determined from large, cumulative annuli with outer radii of  $R_{\text{max}} = R$ . Error bars show the  $1\text{-}\sigma$  dispersion in  $M(r)$  amongst the 1000 projections from which the mean line-of-sight velocity dispersion was computed.

It should be noted that gravitational force softening in the numerical simulation will, necessarily, affect dynamical mass estimates of simulated objects (see, e.g., Tormen, Bouchet & White 1997). That is, on scales smaller than or of order the smoothing length, the mass will be severely overestimated simply due to numerical effects. We have, therefore, restricted our analyses to radii at which the effects of force softening on the mass estimate should be small. In particular, any overestimate of the mass caused by numerical effects is expected to be at most of order 3% to 4% in the innermost radial bins and will drop rapidly to zero for the bins with larger radii.

Cen (1997) and Reblinsky & Bartelmann (1999) have also investigated the virial masses obtained for numerical clusters, though not for objects as massive as those presented here. Reblinsky & Bartelmann (1999) find that the virial mass severely overestimates the true masses of clusters whose masses are less than a few times  $10^{14} M_\odot$ . The degree of overestimation decreases with increasing cluster mass, however, and appears to converge in the mean to the true cluster mass for their most massive objects.

Reblinsky & Bartelmann’s results are broadly consistent with those of Cen (1997), though differences in the procedures used to select and analyse the clusters makes direct comparisons between the two not entirely straightforward. Direct comparisons between our results and those of Cen (1997) and Reblinsky & Bartelmann (1999) are also not straightforward.

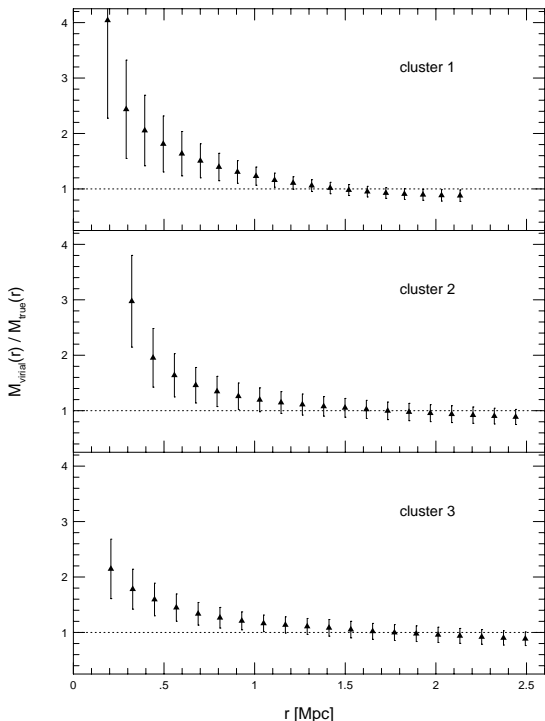


Fig. 12: The 3-dimensional cluster mass profile obtained from the classical virial mass estimator compared to the true cluster mass profile. Particles contained within concentric spheres of radius  $r$  centered on the cluster center of mass were used to determine the mean values of  $R_e$  and  $\sigma_v$  required for the evaluation of equation (13). Error bars show the 1- $\sigma$  dispersion in  $M(r)$  amongst 1000 random projections.

In our analyses above we have expressly calculated  $R_e$  for each of the subsets of the particles, whereas Cen (1997) and Reblinsky & Bartelmann (1999) do not. Also, we have selected our clusters from a 3-dimensional mass distribution while Cen (1997) and Reblinsky & Bartelmann (1999) select their clusters based on 2-dimensional projections and the assignment of luminous galaxies to a random subset of the particles in their simulations. As such, their analyses attempt to at least partially address the issue of contamination by interloper galaxies and false detections of clusters in the limit of realistic observational data. In contrast, our results above are effectively derived in the limit of ideal data (i.e. the values of  $R_e$  and  $\sigma_v^2$  are computed from objects which are known a priori to be contained within the cluster under investigation).

#### 4. DISCUSSION

The cluster mass results which are the most relevant for direct comparison to observational investigations are those that were obtained using large, cumulative annuli (i.e. the shear and particle velocity dispersion averaged over large scales in the cluster) as well as the virial estimate in which  $R_e$  is the effective radius determined for

the “entire” cluster. Although in principle the shear and velocity dispersion can be measured at independent radii in observed clusters, the data are generally too sparse and noisy for this to be practicable. (See, however, Bonnet et al. (1994), Tyson & Fischer (1995), Squires et al. (1996b), Fisher & Tyson (1997) and Carlberg et al. (1997b) for exceptions to this.)

The mass profiles plotted in Figs. 8 through 12 extend to a maximum cluster radius equal to  $r_{200}$  (or  $R_{200}$  in the case of the projected mass profiles). In all cases  $M(r)$  and  $M(R)$  in these figures refer to the mass contained within a 3-dimensional radius,  $r$ , or a projected radius,  $R$ . Since we have defined the clusters to consist of all particles inside of a radius  $r_{200}$ , we will define the total mass of a cluster to be the mass contained within this radius,  $M(r_{200})$ . The total mass obtained for each cluster from each of the estimators is, therefore, indicated by the points in Figs. 8 through 12 that are plotted at the largest occurring values of the radius.

In terms of estimating the total cluster mass (i.e. the mass of the cluster contained within a 3-dimensional radius of  $r_{200}$ ), the classical virial estimator is found to be very successful. The total mass of the cluster is systematically underestimated, but only by  $\sim 10\%$ . This result is somewhat surprising given the fact that within  $r_{200}$  the cluster mass distributions are not perfectly smooth and substructure exists at a significant level. Additionally, moment of inertia analyses performed using all particles within a radius  $r_{200}$  of the cluster centers of mass show the cluster mass distributions to be clearly triaxial, rather than spherical (see Brainerd, Goldberg & Villumsen 1998 for the relevant discussions). Our result, therefore, suggests that at least in the limit of ideal data the classical virial mass estimator is quite robust to modest deviations from pure spherical symmetry and the presence of substructure within a cluster.

The “isothermal” dynamical mass estimate, in which the measured line of sight velocity dispersion is used to infer the mass under the assumption of an isothermal potential, yields a poor estimate of the total mass of the cluster. The value of  $M(r_{200})$  is underestimated by  $\sim 40\%$  for the case in which  $\sigma_v$  is determined from an average over the entire cluster and is underestimated by  $\sim 70\%$  for the case in which  $\sigma_v$  is computed at a projected radius of  $R = R_{200}$  (i.e. Fig. 11).

Provided the mean shear used to infer the cluster velocity dispersion is computed using a large, cumulative annulus in which the shear is averaged over the entire cluster, the weak lensing estimate of  $M(r_{200})$  is found to be in excellent agreement with the total cluster mass (i.e. Fig. 9, open circles). In contrast, however, the shear measured solely at a radius of  $R = R_{200}$  yields a  $\sim 25\%$  overestimate of the total cluster mass (i.e. Fig. 9, solid squares) due to the fact that the clusters are finite in extent, rather than infinite.

Because of its promise to yield direct measurements of the masses of galaxy clusters independent of dynamics and hydrodynamics, weak lensing mass estimates of cluster masses are currently of particular interest. Given the fact that most high-quality observations of the weak lensing shear due to clusters have been obtained only on relatively small scales (i.e. radii significantly less than 1 or 2 Mpc), Figs. 8 and 9 suggest some caution regarding

the interpretation of recent cluster mass estimates that are based on a measurement of an average value of the weak shear together with an assumption of an isothermal cluster potential. In particular, a measurement of the mean shear in which the mean is computed within an aperture whose outer radius is significantly less than  $R_{200}$  yields a mass estimate that differs systematically from the true mass. For example, the projected mass within a radius of 0.5 Mpc,  $M(R = 0.5 \text{ Mpc})$ , is underestimated by  $\sim 40\%$  and the 3-dimensional contained mass,  $M(r = 0.5 \text{ Mpc})$ , is underestimated by  $\sim 35\%$ . Interestingly, in an analysis of observed cluster lensing data, Wu et al. (1998) found that weak lensing mass estimates that were performed over small cluster radii did seem to underestimate the contained mass in a systematic manner.

The results for  $M_{\text{lens}}(r)$  shown in Fig. 9 are, however, encouraging at large cluster radii. In particular, with the advent of large format CCD cameras capable of wide-field imaging, it will be possible to measure the weak shear due to lensing clusters at radii of order a few Mpc in a reasonably routine fashion. An example of such deep wide-field imaging is the data obtained with the UH 8K CCD mosaic camera which has recently resulted in a detection of large scale coherent weak shear in the images of  $\sim 30,000$  faint background galaxies due to lensing by the supercluster MS0302+17 (Kaiser et al. 1998). Given the apparent uni-

versality of the Navarro, Frenk & White density profile (i.e. dissipationless collapse generically leads to the formation of an object with an NFW profile), our results suggest that it will be possible to estimate a total 3-dimensional cluster mass fairly accurately with wide-field imaging simply by computing the mean of the shear over the entire cluster and adopting an isothermal lens potential. In the short term, such observations will hopefully provide a resolution to the remaining discrepancies between cluster masses estimated from weak lensing and virial techniques. (This is, of course, providing that the redshift distribution of the lensed galaxies is well-constrained and is not, in itself, a large source of uncertainty in the interpretation of the observed shear.) In the long term, large surveys from which the weak lensing shear can be detected out to large cluster radii should have the ability to yield uniform samples of objects, including a reasonably accurate mass-selection criterion, without necessarily requiring a full reconstruction of the density profile of each individual lensing cluster.

#### ACKNOWLEDGMENTS

A generous allocation of computing resources on Boston University's Origin2000, support under NSF contract AST-9616968 (TGB and COW) and NSF Graduate Fellowships (DMG and COW) are gratefully acknowledged.

#### REFERENCES

- Bahcall, N. A., Fan, X., & Cen, R. 1997, *ApJ*, 485, L53  
Bahcall, N. A. & Cen, R. 1993, *ApJ*, 407, L49  
Bahcall, N. A., Lubin, L. M. & Dorman, V. 1995, *ApJ*, 447, L81  
Bartelmann, M. 1995, *A&A*, 303, 643  
Bartelmann, M., Narayan, R., Seitz, S. & Schneider, P. 1996, *ApJ*, 464, L115  
Binney, J. & Tremaine, S. 1987, *Galactic Dynamics* (Princeton: Princeton University Press)  
Blandford, R. D., Saust, A. B., Brainerd, T. G., & Villumsen, J. V. 1991, *MNRAS*, 251, 600  
Bonnet, H., Mellier, Y. & Fort, B. 1994, *ApJ*, 427, L83  
Bower, R. G. & Smail, I. 1997, *MNRAS*, 290, 292  
Brainerd, T. G., Goldberg, D. M. & Villumsen, J. V. 1998, *ApJ*, 502, 505  
Bromley, B. C., Warren, M. S., Zurek, W. H., & Quinn, P. J. 1995, *AIP Conference Proceedings* 336, 433  
Bunn, E. & White, M. 1997, *ApJ*, 480, 6  
Carlberg, R. G., Yee, H. K. C. & Ellingson, E. 1994, *ApJ*, 437, 63  
Carlberg, R. G., Yee, H. K. C. & Ellingson, E. 1997, *ApJ*, 478, 462  
Carlberg, R. G., Yee, H. K. C., Ellingson, E., Abraham, R., Gravel, P., Morris, S., & Pritchet, C. J. 1996, *ApJ*, 462, 32  
Carlberg, R. G., Yee, H. K. C., Ellingson, E., Morris, S. L., Abraham, R., Gravel, P., Pritchet, C. J., Smecker-Hane, T., Hartwick, F. D. A., Hesser, J. E., Hutchings, J. B., & Oke, J. B. 1997a, *ApJ*, 476, L7  
Carlberg, R. G., Yee, H. K. C., Ellingson, E., Morris, S. L., Abraham, R., Gravel, P., Pritchet, C. J., Smecker-Hane, T., Hartwick, F. D. A., Hesser, J. E., Hutchings, J. B., & Oke, J. B. 1997b, *ApJ*, 485, L13  
Cen, R. 1997, *ApJ*, 485, 39  
Cole, S. M. & Lacey, C. G. 1996, *MNRAS*, 281, 716  
Dahle, H., Maddox, S. J. & Lilje, P. B. 1994, *ApJ*, 435, L79  
David, L. P., Jones, C. & Forman, W. 1995, *ApJ*, 445, 578  
Dubinski, J. & Carlberg, R. 1991, *ApJ*, 378, 496  
Eke, V. R., Cole, S. & Frenk, C. S. 1996, *MNRAS*, 282, 263  
Fahlman, G., Kaiser, N., Squires, G. & Woods, D. 1994, *ApJ*, 289, L1  
Fan, X., Bahcall, N. & Cen, R. 1997, *ApJ*, 415, L17  
Fischer, P., Bernstein, G., Rhee, G., & Tyson, J. A. 1997, *ApJ*, 113, 521  
Fischer, P. & Tyson, J. A. 1997, *AJ*, 114, 14  
Ghigna, S., Moore, B., Governato, F., Lake, G., Quinn, T., & Stadel, J. 1998, *MNRAS*, 300, 146  
Gott, J. R. & Turner, E. L. 1976, *ApJ*, 209, 1  
Gunn, J. E. 1978, in *Observational Cosmology*, ed. A. Maeder, L. Martinet, & G. Tammann (Sauverny: Geneva Obs.), 1  
Kaiser, N. 1995, *ApJ*, 439, L1  
Kaiser, N. & Squires, G. 1993, *ApJ*, 404, 441  
Kaiser, N., Squires, G. & Broadhurst, T. 1995, *ApJ*, 449, 460  
Kneib, J.-P., Ellis, R. S., Smail, I., Couch, W. J., & Sharples, R. M. 1996, *ApJ*, 471, 643  
Kaiser, N., Wilson, G., Luppino, G., Kofman, L., Gioia, I., Metzger, M., & Dahle, H. 1998, *ApJ* submitted (astro-ph/9809268)  
Lubin, L. M. & Bahcall, N. A. 1993, *ApJ*, 415, L17  
Luppino, G. & Kaiser, N. 1997, *ApJ*, 475, 20  
Mellier, Y., Dantel-Fort, M., Fort, B., & Bonnet, H. 1994, *A&A*, 289, L15  
Miralda-Escudé, J. & Babul, A. 1995, *ApJ*, 449, 18  
Navarro, J. F., Frenk, C. S. & White, S. D. M. 1995, *MNRAS*, 275, 720  
Navarro, J. F., Frenk, C. S. & White, S. D. M. 1996, *ApJ*, 462, 563  
Navarro, J. F., Frenk, C. S. & White, S. D. M. 1997, *ApJ*, 490, 493  
Oaxaca Wright, C. & Brainerd, T. G. 1999, in preparation  
Ramella, M., Geller, M. J. & Huchra, J. P. 1989, *ApJ*, 344, 57  
Reblinsky, K. & Bartelmann, M. 1999, *A&A*, in press (astro-ph/9902153)  
Schneider, P. 1995, *A&A*, 302, 639  
Schneider, P., Ehlers, J., & Falco, E. E. 1992, *Gravitational Lensing* (Berlin: Springer-Verlag)  
Schneider, P. & Seitz, C. 1995, *A&A*, 294, 411  
Schwarzschild, M. 1954, *AJ*, 59, 273  
Seitz, C. & Schneider, P. 1995, *A&A*, 297, 287  
Seitz, C., Kneib, J.-P., Schneider, P., & Seitz, S. 1996, *A&A*, 314, 707  
Seitz, S. & Schneider, P. 1996, *A&A*, 305, 383  
Seitz, S., Schneider, P. & Bartelmann, M. 1998, *ApJ*, 337, 325  
Smail, I. & Dickinson, M. 1995, *ApJ*, 455, L99  
Smail, I., Ellis, R. S., Fitchett, M. J. 1994, *MNRAS*, 270, 245  
Smail, I., Ellis, R. S., Fitchett, M. J., & Edge, A. C. 1995, *MNRAS*, 273, 277  
Smail, I., Ellis, R. S., Dressler, A., Couch, W., Oemler, A., Sharples, R. M., & Butcher, H. 1997, *ApJ*, 479, 70  
Smith, S. 1936, *ApJ*, 83, 29  
Squires, G. & Kaiser, N. 1996, *ApJ*, 473, 65  
Squires, G., Kaiser, N., Babul, A., Fahlman, G., Woods, D., Neumann, D. M., & Böhringer, H. 1996a, *ApJ*, 461, 572  
Squires, G., Kaiser, N., Fahlman, G., Babul, A., & Woods, D. 1996b, *ApJ*, 469, 73  
Tormen, G., Bouchet, F. & White, S. D. M. 1997, *MNRAS*, 286, 865  
Tyson, J. A., Wenk, R. A. & Valdes, F. 1990, *ApJ*, 349, L1  
Tyson, J. A. & Fischer, P. 1995, *ApJ*, 466, L55  
Waxman, E. & Miralda-Escudé, J. 1995, *ApJ*, 451, 451

- White, S. D. M., Efstathiou, G. & Frenk, C. S. 1993, MNRAS, 262, 1023
- Viana, T. P. & Liddle, A. R. 1996, MNRAS, 281, 323
- Villumsen, J. V. 1989, ApJS, 71, 407
- Wu, X.-P., Chiueh, T., Fang, L.-Z., & Yan-Jie, X. 1998, MNRAS, in press
- Zwicky, F. 1933, Helv. Phys. Acta, 6, 110
- Zwicky, F. 1937, ApJ, 86, 217

This figure "fig1.jpg" is available in "jpg" format from:

<http://arxiv.org/ps/astro-ph/9903069v1>

This figure "fig2.jpg" is available in "jpg" format from:

<http://arxiv.org/ps/astro-ph/9903069v1>

This figure "fig3.jpg" is available in "jpg" format from:

<http://arxiv.org/ps/astro-ph/9903069v1>